APPLIED PHYSICS

Self-powered visualized tactile-acoustic sensor for accurate artificial perception with high brightness and record-low detection limit

Li Su[1,2]†, Shuangyang Kuang[3]†, Yong Zhao[1,2]*, Junhuan Li[1], Guodong Zhao[1], Zhong Lin Wang[4,5]*, Yunlong Zi[6,7,8]*

The growth of the Internet of Things has focused attention on visualized sensors as a key technology. However, it remains challenging to achieve high sensing accuracy and self-power ability. Here, we propose a self-powered visualized tactile-acoustic sensor (SVTAS) based on an elaborated triboelectrification-induced electroluminescence (TIEL) unit. To date, it features a high brightness of 0.5 mW cm^{-2} (32 cd m^{-2}) and a record-low detection limit of 0.5 kPa in horizontal-sliding mode. Meanwhile, the SVTAS is applicable to convert acoustic waves into TIEL signals in contact-separation mode, showing the highest response to the 44.07 Hz sound, a high signal-to-noise ratio of 8.7 dB^{-1}, and an ultrafast response time of 0.8 ms. Furthermore, advanced artificial visualized perception systems are constructed with excellent performance in recognizing motion trajectories and human speech with different words/sentences. This work paves the way for the highly efficient and sustainable development of new-generation self-powered visualized perception systems, contributing a solution to wireless communication free from electromagnetic interference.

INTRODUCTION

With the close coordination between the eyes and the brain, visual information can be detected and preprocessed by the retina and then transmitted to the visual cortex for further complex perceptual processing. Therefore, an artificial visualized perception system is requisite and essential for artificial intelligence and human-machine interactions (HMIs) (*1*, *2*). In comparison, traditional artificial perception systems based on different types of electrical sensors normally suffer from complicated circuits and electromagnetic interference (*3*–*11*), which is adverse to most Internet of Things (IoT) applications where high data throughput and limited energy supply are common. Under these circumstances, self-powered visualized sensors can be used to emulate the artificial visualized perception system by integrating the functions of self-luminescent sensors and artificial synapses, which is based on human-readable visible optical signals without electrical wire connections and free of electromagnetic interference, thus providing an alternative communication approach (*12*–*18*). So far, mechanoluminescence (ML) has become one of the most representative techniques applied to produce self-powered visualized sensors due to its fast response to mechanical stimulus, drawing a great deal of attention for research (*19*–*22*). However, there are still some outstanding problems that arise from the high-accuracy recognition based on this technique. On the one hand, the triggering threshold is too high to detect gentle mechanical stimuli sensing such as acoustic waves (*23*–*26*). On the other hand, the low luminescent intensity affects portability under illumination, which limits the scope of application (*27*, *28*). Therefore, the poor sensitivity of ML has become a major constraint on its application, which necessitates the development of innovative sensing technology.

Most recently, it has been discovered that the triboelectrification-induced electroluminescence (TIEL) based on triboelectrification and electroluminescence (EL) effect can convert gentle mechanical stimuli into real-time light emission, which can be proposed as a novel form of ML and provides an alternative to the development of visualized sensors (*29*–*36*). When two different materials are in dynamic interaction with each other, the surface charges generated by the triboelectric effect at their interfaces produce a fast-changing electric field in the EL material. Thus, highly efficient EL is achieved with such characteristics as simplified structure, low triggering threshold, high responsivity, excellent repeatability, and stability (*37*–*40*). In particular, it is revealed that TIEL allows for a wide material selection to generate triboelectricity and a more versatile structure, which is beneficial for optimization of the components and architectures of the composite material (*41*–*48*). As a result, TIEL has the potential for ultrasensitive mechanical sensing in various settings, especially the artificial visualized perception system.

In this work, a self-powered visualized tactile-acoustic sensor (SVTAS) is developed through a TIEL unit for real-time artificial perception. Because of the polarization/modulus regulation and the unique interfacial charge trapping ability of the mesh electrode–enhanced layer, a high brightness of 0.5 mW cm^{-2} (32 cd m^{-2}) and the ultralow detection limit at 0.5 kPa are achieved in horizontal-sliding (HS) mode, with the light emission observable even under

[1]Hebei Key Laboratory of Micro-Nano Precision Optical Sensing and Measurement Technology, School of Control Engineering, Northeastern University at Qinhuangdao, Qinhuangdao, Hebei 066004, China. [2]College of Information Science and Engineering, Northeastern University, Shenyang, Liaoning 110819, China. [3]Hubei Key Laboratory of Plasma Chemistry and Advanced Materials, School of Materials Science and Engineering, Wuhan Institute of Technology, Wuhan, Hubei 430205, China. [4]Beijing Institute of Nanoenergy and Nanosystems, Chinese Academy of Sciences, Beijing 101400, China. [5]College of Materials Science and Engineering, Georgia Institute of Technology, Atlanta, GA 30332, USA. [6]Thrust of Sustainable Energy and Environment, The Hong Kong University of Science and Technology (Guangzhou), Nansha, Guangzhou, Guangdong 511400, China. [7]HKUST Shenzhen-Hong Kong Collaborative Innovation Research Institute, Futian, Shenzhen, Guangdong 518048, China. [8]Guangzhou HKUST Fok Ying Tung Research Institute, Nansha, Guangzhou, Guangdong 511457, China.
*Corresponding author. Email: zhaoyong@ise.neu.edu.cn (Y.Zhao); zlwang@binn.cas.cn (Z.L.Y.); ylzi@hkust-gz.edu.cn (Y.Zi)
†These authors contributed equally to this work.

an ambient illumination of 300 lux. Meanwhile, the SVTAS is capable of converting acoustic waves into TIEL signals in contact-separation (CS) mode, showing the highest response to the 44.07 Hz sound, a high signal-to-noise ratio (SNR) of 8.7 dB^{-1}, and an ultrafast response time of 0.8 ms at 60 to 90 dB. Compared with various TIEL-related works, the SVTAS features the highest brightness and the lowest detection limit. Furthermore, real-time artificial visualized perception systems are demonstrated for the highly accurate recognition of motion trajectories and human speech with different words/sentences. Therefore, the proposed SVTAS is expected not only to promote the development of self-powered visualized sensors but also to expand the scope of application notably for TIEL.

RESULTS

Overview of the SVTAS

Figure 1A illustrates the structure of the SVTAS, which features a layer-by-layer configuration. In design, the SVTAS is composed of a triboelectrification layer made of polyvinylidene difluoride (PVDF) nanofibers, a flexible luminescent layer consisting of the ZnS:Cu embedded in polymethyl methacrylate (PMMA) (ZEPM) film, a transparent mesh electrode–enhanced layer, and a substrate. The preparation of SVTAS is detailed in Materials and Methods and fig. S1. The SVTAS enables the conversion of gentle touch and sound stimuli into TIEL signals without any external power supply under HS and CS mode, respectively. Therefore, versatile artificial visualized perception systems are developed by using the SVTAS, a signal acquisition unit [photodetector or charge-coupled device (CCD) camera], and a processing unit (artificial neural network) for highly accurate intelligent control and speech recognition. Figure 1B shows the design of SVTAS. Specifically, PMMA is adopted as the matrix of the luminescent layer owing to the ease of crystallization, high optical transmittance, and the significant difference in triboelectric polarity with the fluoropolymers (Fig. 1, B and I). Moreover, the electrospinning nanofibers with high Young's modulus (PVDF nanofibers in this case) can act as the triboelectrification layer and vibrating membrane to facilitate the generation of tribo-charges and the absorption of acoustic waves (Fig. 1B, II). Moreover, the tribo-charges can be trapped on the edges of the mesh electrode during the triboelectrification process, leading to a significant improvement of interfacial trap density that will be introduced in the later section (Fig. 1B, III). On this basis, unprecedented high-luminescence and low-threshold value can be obtained in SVTAS. The quantitative sensing measurement system is illustrated in figs. S2 and S3 and text S1. The TIEL emission has a high brightness of 0.5 mW cm^{-2} (32 cd m^{-2}) under HS mode, which is discernible to an ambient illumination of 300 lux (Fig. 1C and text S2). Meanwhile, the SVTAS converts acoustic waves into TIEL signals under CS mode, indicating its response with a threshold at the sound pressure level (SPL; Fig. 1D). Thus, the SVTAS-based artificial visualized perception system with TIEL-enabled transmission is expected to promote a new generation of optical communication in the field of IoTs without any electromagnetic interference, as illustrated in Fig. 1E.

The geometrical design of the mesh electrode–enhanced layer

The well-designed electrode structure is beneficial for generating a high and fast-changing electric field, which can improve the TIEL sensitivity significantly (*39*, *40*). Therefore, the geometrical design of the mesh electrode–enhanced layer is further refined to improve the TIEL intensity. Figure 2A illustrates the working mechanism of the SVTAS under HS mode, which relies on the coupling of triboelectrification and EL effects. There are four major states in one working cycle with the mesh electrode–enhanced layer simplified to two arbitrary coplanar electrodes (E_1 and E_2). When an external object moves, such as PVDF nanofibers moving against the luminescent layer, the luminescent layer is positively charged, while the surface of the PVDF nanofibers is negatively charged because of their triboelectric polarity difference. In the initial state I, with the moving object on the left side, the tribo-charges can produce a rightward electric field. If it moves forward to the middle (states II and IV), the tribo-charges generate no electric field due to an equal electric potential between the two electrodes. As it further moves to the right side, a leftward electric field is generated (state III). In this way, the back-and-forth movement leads to an alternating electric field with fast changes in amplitude and direction. Thus, the underlying EL phosphors are excited to generate the TIEL with a peak value of 520 nm in the spectrum (fig. S4). To fully understand the above working mechanism, a further investigation was conducted through the numerical simulation assisted by the software package COMSOL Multiphysics. The two-dimensional (2D) models without and with electrodes were constructed for the cross-sectional view of electric field distribution in the four working states as discussed in Fig. 2B and text S3, with the dimensions comparable to an actual device. To simplify the simulation process, two coplanar electrodes (E_1 and E_2) with a unit size of a thickness of 100 μm and a width of 4 mm were used. Notably, in the presence of electrodes (Fig. 2B, II), the electric field was strengthened on the electrodes' edge, which implies higher efficiency and stronger EL than in the absence of electrodes (Fig. 2B, I). The results show that TIEL intensity can be further improved by optimizing the gap/breadth (*G*/*D*) ratio of the electrodes with the same area (12 mm × 12 mm) and number of units (2 × 2), as shown in Fig. 2C. In the course of COMSOL simulation, the amplitudes of the electric field along the black dash line on the luminescent layer were extracted in the four working states, respectively (fig. S5). It was found that the electric field variation in the nonelectrode case was smooth and the amplitude was limited (Fig. 2D). The SVTAS with five different *G*/*D* ratios (1/4.5, 2/4, 3/3.5, 4/3, and 5/2.5) was investigated separately to reveal the influence of the *G*/*D* ratio on the TIEL intensity in four states, respectively, as shown in Fig. 2 (E to G). It was discovered that a significantly enhanced electric field was generated in the edge regions near the electrodes, which is consistent with the observations in previous studies (*39*, *40*). In one working cycle, the electric field variation on the phosphors (ΔE) reached a maximum of 4.89 MV m^{-1}, which is almost three times as high as that without electrodes (1.53 MV m^{-1}) (fig. S6). Nevertheless, it is worth mentioning that the enhanced luminescent regions are mainly concentrated on the electrodes, which is contracted with the increase in *G*/*D* ratio. By using these two interdependent factors, an optimum *G*/*D* ratio of 2/4 is determined for the maximum TIEL intensity (Fig. 2H). It is found that the SVTAS with optimum mesh electrode layer has a significantly improved TIEL intensity (about 2.5-fold) and reaches saturation much faster than the SVTAS without electrodes, as shown in Fig. 2I. These results not only support the geometrical design of the mesh electrode–enhanced layer but also confirm its enhanced performance in interfacial trap density.

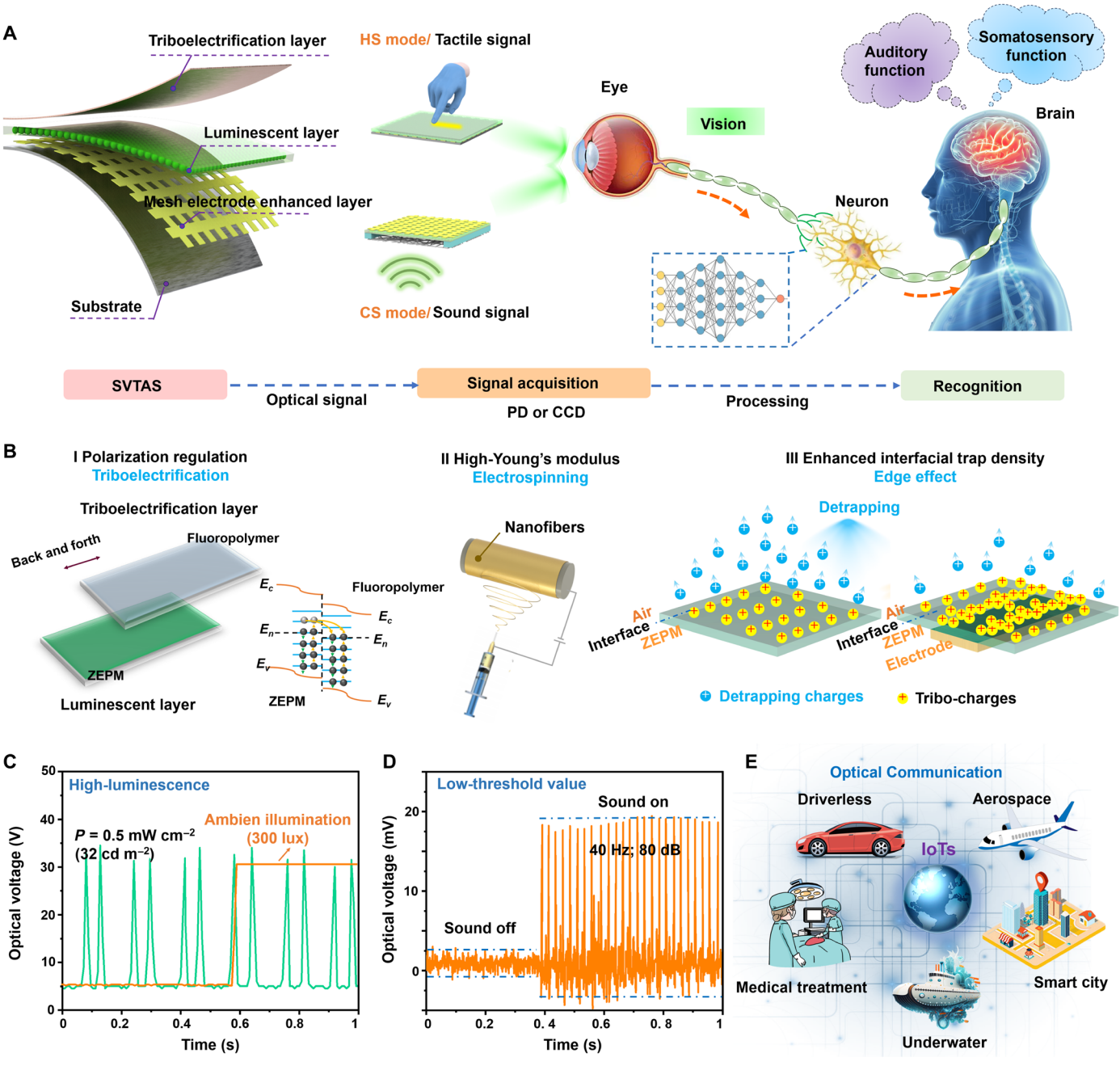

Fig. 1. Structural design and application of SVTAS. (**A**) The layer-by-layer structure of SVTAS and the schematic diagram of tactile-acoustic sensing by an artificial visualized perception system under HS and CS mode, respectively. (**B**) Schematic diagram of the design process of SVTAS. (I) Polarization regulation in triboelectrification (inset: schematic of triboelectric mechanism), (II) the nanofibers with high Young's modulus as acquired by electrospinning, and (III) the interfacial trap density improved by edge effect of the electrodes. Typically measured optical voltage from SVTAS under (**C**) tactile and (**D**) sound stimuli, indicating the high-luminescence and low-threshold value. (**E**) Application of SVTAS in optical communication in IoTs.

Tactile sensing properties of SVTAS

The TIEL intensity of SVTAS under HS mode for tactile sensing was analyzed by adjusting several variables, including ZnS:Cu content, material type, and the motion frequency of the triboelectrification layer, as well as the pressure at the contact surface. First, the maximum TIEL intensity was achieved at the optimal mass ratio (50 wt %) of ZnS:Cu phosphors in the whole ZEPM film (Fig. 3A). Otherwise, the excessively high content of ZnS:Cu phosphors can reduce the contact electrification of the ZEPM film and suppress tribo-charges generation. Second, it was found out that the TIEL intensity increased accordingly with the variation in triboelectric polarity between the triboelectrification layer and PMMA polymer, as shown in Fig. 3B. Thus, PVDF nanofibers were taken as the triboelectrification layer to achieve an excellent TIEL performance in

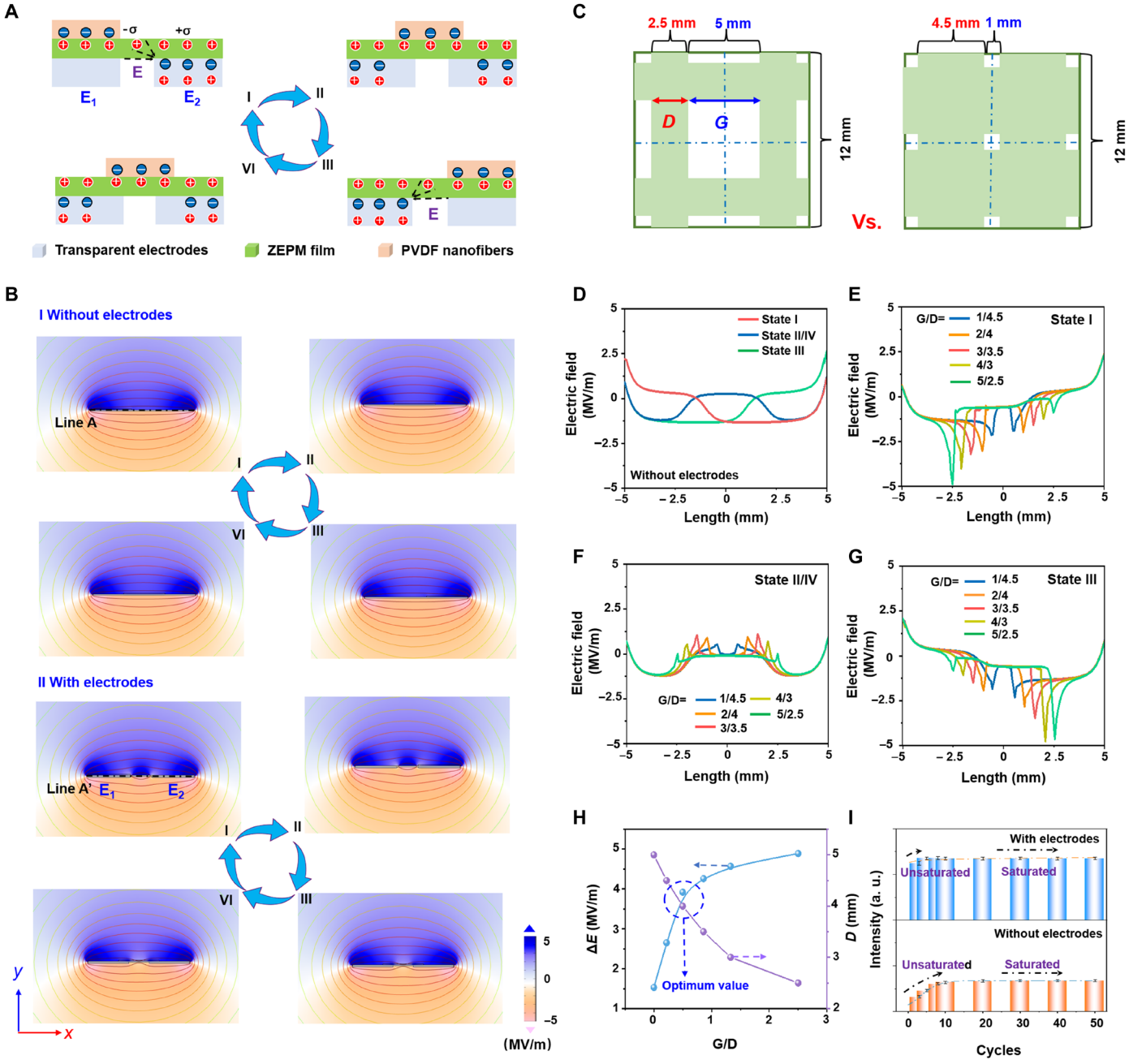

Fig. 2. The geometrical design of the mesh electrode–enhanced layer. (**A**) Working mechanism of SVTAS applied by the mesh electrode–enhanced layer when the moving external object is in four different states. (**B**) The 2D electric field distribution of SVTAS (I) without and (II) with electrodes in the four working states as revealed by COMSOL simulation. (**C**) The comparison of the mesh electrode layer with the same unit size (12 mm × 12 mm) and the different *G/D* ratios (*G/D*s are 5/2.5 and 1/4.5), respectively. (**D**) The 1D electric field distribution along the black dash line on the luminescent layer of the four different states in the absence of electrodes in (B), I. The 1D electric field distribution along the black dash line on the luminescent layer with the different *G/D* ratios of the four different states (**E**) state I, (**F**) state II/IV, and (**G**) state III in the presence of electrode, respectively. (**H**) The optimum *G/D* ratio of the unit size in the mesh electrode–enhanced layer. (**I**) TIEL intensity of SVTAS increased with the rubbing cycles, indicating that the mesh electrode layer increased the interfacial trap density to reach the maximum rapidly.

this case due to its highly negative electricity, large surface areas, and modulable Young's modulus. In addition, TIEL intensity was enhanced with an increase in motion frequency of PVDF nanofibers from 1 to 12 Hz, which is attributed to a rise in the number of moving cycles of electrons in ZnS:Cu phosphors activating the luminescence centers within a unit time interval (Fig. 3C and fig. S7). Furthermore, the TIEL intensity of SVTAS increased with the pressure ranging from 0.5 to 50 kPa at 8 Hz, and the sensitivity was divided into three regions (*49*, *50*). This is attributed to the contact between the ZEPM film and PVDF nanofibers (Fig. 3E and figs. S8 and S9). In the low-pressure region from 0.5 to 25 kPa, the expansion of contact area is caused by the elastic deformation of soft texture,

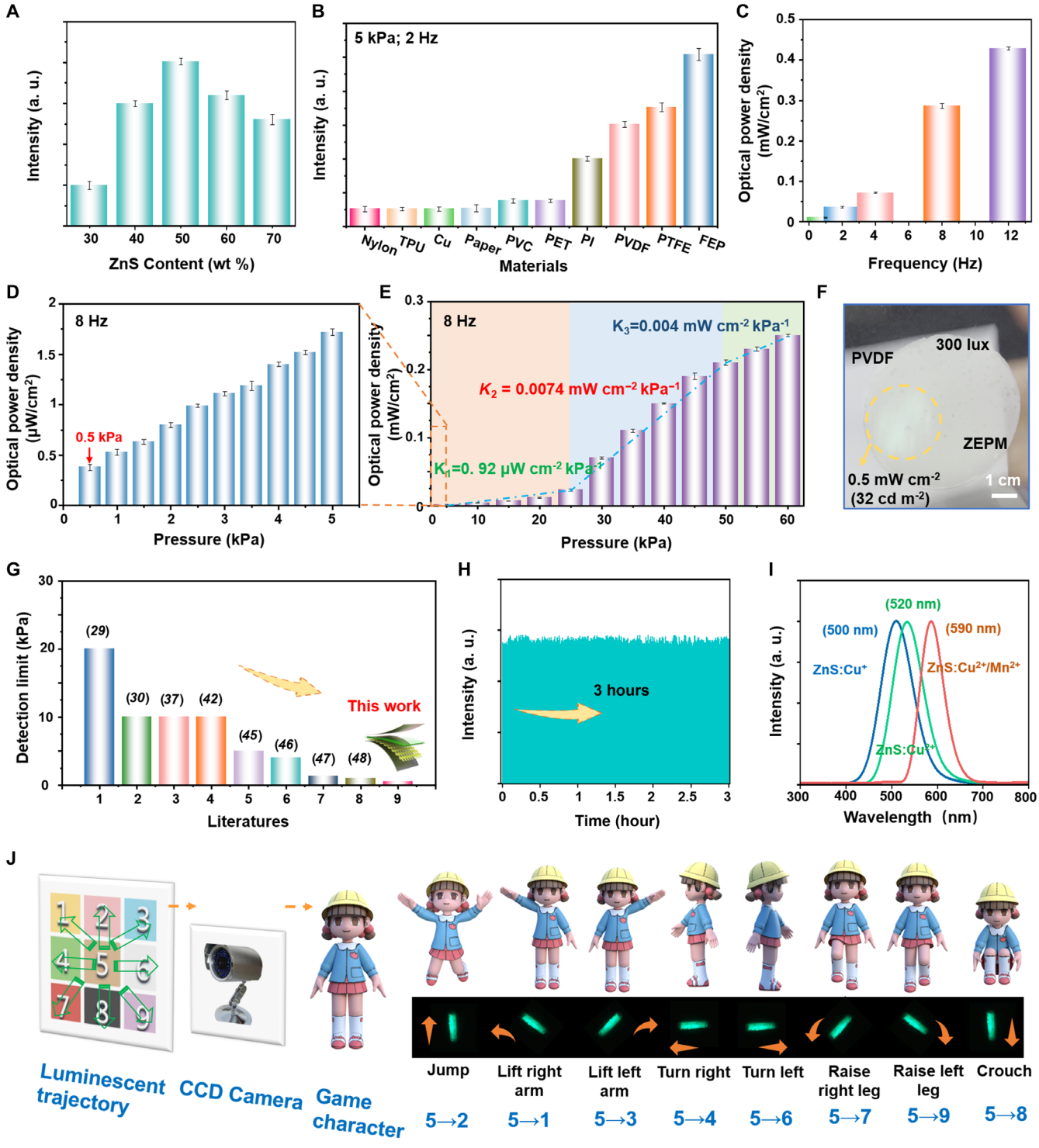

Fig. 3. Tactile-TIEL responsive performance of SVTAS under HS working mode. TIEL intensity with (**A**) a varied ZnS:Cu content, (**B**) different triboelectrification materials at 5 kPa and 2 Hz, (**C**) an increase in sliding frequency from 1 to 12 Hz at a pressure of 50 kPa by using PVDF nanofibers as the sliding object, (**D**) a rise in pressure from 0 to 5 kPa at an interval of 0.5 kPa, showing a trigger pressure threshold of as low as 0.5 kPa, and (**E**) an increase of pressure in a larger range from 0 to 50 kPa with an interval of 5 kPa. (**F**) TIEL image of SVTAS in an ambient illumination of 300 lux. (**G**) The comparison in trigger pressure threshold between the SVTAS proposed in this work and other TIEL materials. (**H**) Stability and repeatability test of the TIEL emission in 3 hours at an interval of 500 ms. (**I**) TIEL spectra of SVTAS embedded with different color electroluminescent powers ($ZnS:Cu^{+}$, $ZnS:Cu^{2+}$, and $ZnS:Cu^{2+}/Mn^{2+}$). (**J**) Demonstration of the SVTAS as a tactile sensor for amusement games.

which causes a slow improvement of TIEL intensity with the increase in contact pressure at a pressure sensitivity of 0.92 μW cm^{-2} kPa^{-1}. In the medium-pressure region from 25 to 50 kPa, the nanostructures on the PVDF fibers make the nanoscale elastic deformation effective in expanding the actual contact area significantly with the increase in pressure, which leads to a very high sensitivity of 0.0074 mW cm^{-2} kPa^{-1}. While in the high-pressure region beyond 50 kPa, high pressure is the dominant factor instead of the contact area, thus causing the rise in TIEL intensity to slow down with a pressure sensitivity of 0.004 mW cm^{-2} kPa^{-1}. Notably, TIEL emission was clearly observed even in an ambient illumination of 300 lux (Fig. 3F and movie S1). Moreover, it is noteworthy that the trigger pressure threshold of SVTAS reached as low as 0.5 kPa (Fig. 3D), which is the minimum in TIEL materials ever reported (Fig. 3G and table S1). Furthermore, the repeatability and stability of the TIEL emission were evaluated for 3 hours at an interval of 500 ms, revealing a stable TIEL emission of the SVTAS, as shown in Fig. 3H. Besides, the different EL phosphors in ZEPM film were found to show various luminescent colors (green-blue, green, and orange), indicating the applicability of SVTAS to sense the external stimuli with colorful luminescence (Fig. 3I). On this basis, an advanced artificial visualized perception system was developed with the assistance of a CCD camera and a self-developed software (programmed by Python) for the TIEL-enabled game intelligent control system. Depending on the trajectory captured by the camera, the game character moved accordingly, which confirms the feasibility of this tactile sensing system (Fig. 3J, text S4, and movie S2).

Acoustic sensing properties of SVTAS

Figure 4A illustrates the rationale of acoustic sensing by SVTAS under CS mode. Specifically, the propagation of the acoustic wave induces the difference in air pressure between two sides of the PVDF nanofiber membrane, thus causing the periodical vibration of the membrane. The periodical vibration of the membrane causes CS triboelectrification between the PVDF membrane and ZEPM films, which completes a working cycle of TIEL generation with four working states similar to the HS mode. A simulation of deformation-induced displacement of the circular PVDF nanofiber membrane at four different acoustic frequencies through COMSOL Multiphysics is shown in Fig. 4B and text S5. According to the simulation results for the PVDF nanofiber membrane with a diameter of 6 cm and a thickness of 100 μm, there are different vibration modes created at a certain acoustic frequency and the resonance frequency appears at 44.044 Hz in the first-order vibration mode, which usually indicates the most significant mechanical deformation. Furthermore, the sensing performance and the characteristics of basic SVTAS with different geometric parameters were systematically investigated. For SVTAS, diameter (D_m), thickness (T_m), and gap distance (G_m) are three critical parameters affecting the frequency response. As revealed by the experiments and finite element analysis, larger D_m and T_m lead to a lower resonant frequency (figs. S10 and S11). Moreover, an appropriate G_m ensures not only the contact between the PVDF nanofibers and the ZEPM film but also the charge replenishment during operation (fig. S12). These theoretical analyses provide crucial guidance on obtaining a stable SVTAS with modulating frequency. Thus, the TIEL signal of SVTAS (D_m = 6 cm, T_m = 100 μm, and G_m = 100 μm) was measured in response to a fixed frequency of piano keys or a speaker with continuous waves, as shown in Fig. 4C. The sounds of piano keys from C1 to A1 with a SPL of 80 dB were recorded by the kinetic curve of the TIEL peak and a commercial acoustic-electric sensor for comparison (fig. S13). The TIEL intensity was found to reach its maximum when the key of F1 was pressed, indicating a resonance frequency of approximately 43.7 Hz (Fig. 4D). This is consistent with the simulation results (Fig. 4B). As shown in Fig. 4E, the piano key sounds (D1, E1, F1, and G1) are recorded four times by monitoring the TIEL peaks, demonstrating the high repeatability of the SVTAS for acoustic sensing. Notably, when the three keys were pressed simultaneously (Fig. 4, F and H), the frequency spectra of SVTAS appeared as three key frequencies according to the Fourier transform (Fig. 4, G and I). Moreover, the directional sound response is shown in Fig. 4J. The directional pattern shows the mirror symmetry, which provides a wide-angle range for acoustic sensing. In the experiment of SPL sensing, the sounds with varied SPL from 60 to 90 dB were recorded to fit the exponential relationship with a high sensitivity of 1.4 mV dB^{-1} in the region of 85 to 90 dB (Fig. 4K). Besides, the kinetic curve of TIEL peak was distinguished from the noise with an interval of 25 ms at the sound frequency of 40 Hz, showing an ultralow response time of 0.8 ms, as shown in Fig. 4L. The SNR can be calculated to be 8.7 dB^{-1} (fig. S14A). Furthermore, considering the range of 20 to 20,000 Hz in the frequency of audible sound waves for humans, textual information was also recognized by the SVTAS. The pronouncing optical signal curves of Chinese pinyin of "e, f, and g" and English letters of "A and B" were recorded (fig. S14, B and C). Thus, if the transmitted control signal is modulated by digits "0" and "1," digital information can be transmitted by the optical signal of the SVTAS, and optical signal communication can be achieved.

Speech recognition application of SVTAS

By taking advantage of the unique acoustic-TIEL responsive performance of SVTAS, an advanced artificial visualized perception system is proposed for speech recognition through a convolutional neural networks (CNNs) model (fig. S15 and text S6) to classify different words and sentences, as shown in Fig. 5 (A and I). First, adjusting the amplitudes and frequencies of human speech makes it possible to obtain a series of luminescent images from SVTAS with varied brightness and different shapes, as demonstrated by the COMSOL stimulation in Fig. 4B and movie S3. Then, the adaptive threshold segmentation method is used to extract the effective image data (Fig. 5A, II). Afterward, the data are input into the CNN for feature extraction (Fig. 5A, III), thus learning the hidden semantics in acoustic waves of human speech. Through the proposed CNN model, a variety of application scenarios can be realized, such as HMI or a new-type hearing aid (Fig. 5B and movie S4). The obtained luminescent images of the five command words collected by SVTAS (including "jump," "run," "squat," "stand," and "walk") are input into the CNN model to train the model. Figure 5C shows the typical exemplary set of the actual luminescent images of SVTAS corresponding to the five command words with significant differences in luminescent shapes. The model parameters are extracted in the training process at once until the loss function value ceases to decrease while the prediction accuracy shows no more improvement (fig. S16). By using the test dataset for validation, the confusion matrix of the five command words can be obtained, as shown in Fig. 5D. It is demonstrated that the CNN model proposed in this article achieves high accuracy and

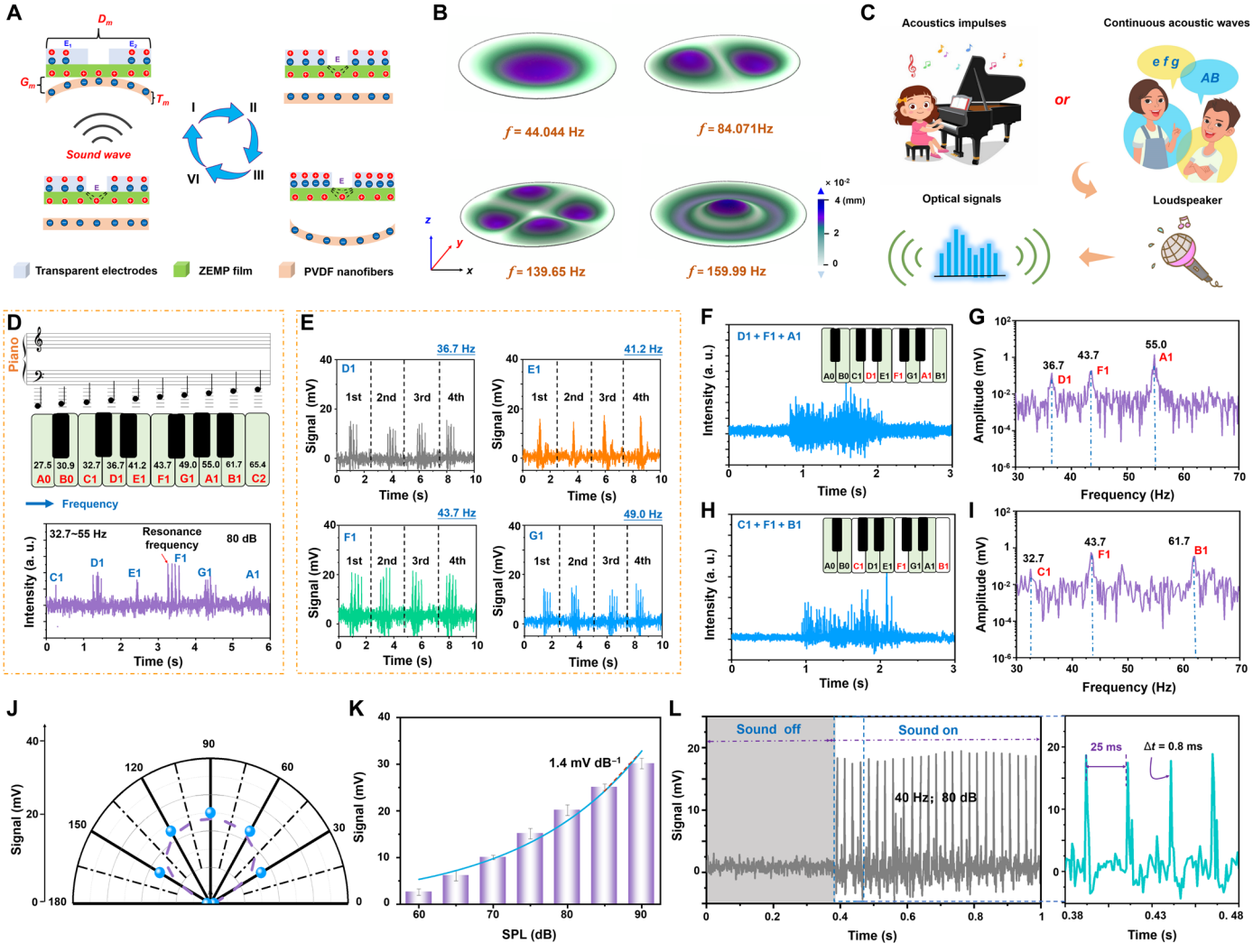

Fig. 4. Acoustic-TIEL responsive performance of SVTAS under CS working mode. (**A**) Cross-sectional scheme of the working mechanism of SVTAS under CS mode for acoustic sensing. (**B**) The vibration mode of PVDF nanofiber circular membrane at different frequencies along with *z* displacement by COMSOL simulation. (**C**) The schematic diagram shows the measurement of the acoustic response of optical signals, in which the SVTAS is placed near a loudspeaker. The impulse sound wave is generated from a piano and the continuous sound waves are generated from a speaker. (**D**) The optical voltage of the SVTAS versus piano key frequency at 80 dB, indicating the resonance frequency around F1. (**E**) Four times of repetitive optical signal measurement of monitoring the piano key of D1, E1, F1, and G1, respectively. The optical voltage signals measured when three piano keys (**F**) D1 + F1 + A1 and (**H**) C1 + F1 + D1 are pressed simultaneously, and their corresponding frequency spectrum (**G**) and (**I**) captured through Fourier transform. (**J**) The direction sound response property of testing angles from 0° to 180°. (**K**) The acoustic response of an SVTAS under various sound intensities. (**L**) Difference in acoustic response between the noise and specific continuous sound signal (around 40 Hz and 80 dB). Right: The enlarged view of the response signals indicates the fast response time of SVTAS, which is defined as the duration time from the noise to the maximum.

strong robustness. Furthermore, this proposed model also suits some scenarios where communication is hindered, such as between doctors and patients on nuclear magnetic resonance scan, as illustrated in Fig. 5E. Although the acoustic waves of sentences have a longer duration and lower purity effective information than the words, after similar data processing by the CNN model (fig. S17), the normalized confusion matrix of the six sentences from the SVTAS (Fig. 5, F and G) indicates that the CNN model can also achieve a high classification accuracy in sentence semantic recognition, as shown in Fig. 5H. Therefore, the SVTAS is promising for the development of a new hearing system with outstanding sensing performance, which may be the focus of future research on self-luminescent functional sensors.

DISCUSSION

The application of visualized sensors has recently been popularized because of their wireless communication, visible light feedback, and extraordinary electromagnetic-free interference in the IoTs. However, it remains challenging to achieve high sensing accuracy and

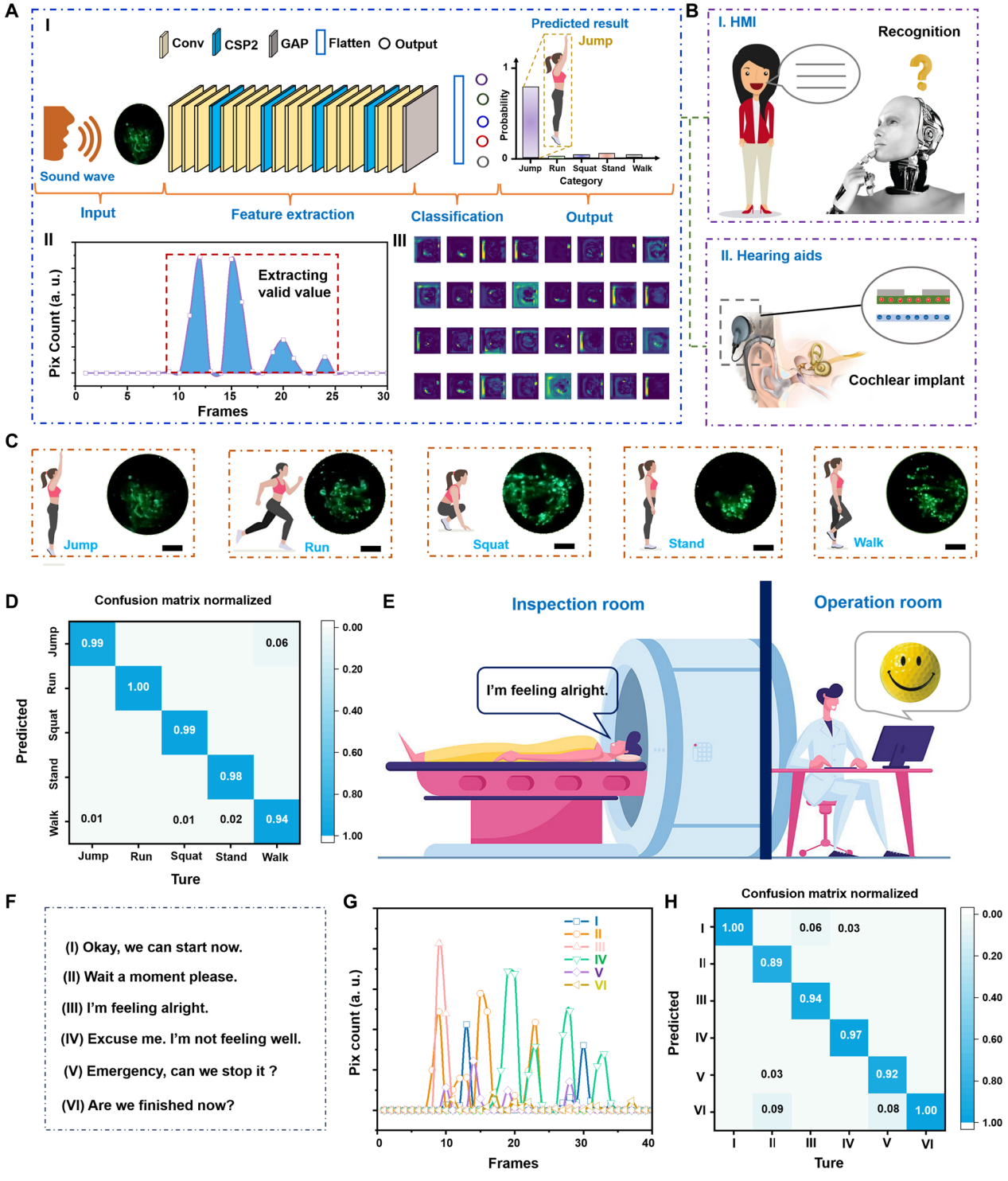

Fig. 5. The speech recognition application of SVTAS. (**A**) Illustration of CNN for speech recognition. (I) Structure of CNN, (II) luminescent pix count from SVTAS in typical image sequence, and (III) visualization of luminescence features extracted by CNN. (**B**) Proposed application of SVTAS in (I) HMI and (II) hearing aids. (**C**) A typical exemplary set of the actual luminescent images of SVTAS corresponding to the five command words. Scale bars, 1 cm. (**D**) Classification test normalized confusion matrix for recognizing the five words in (C). (**E**) Proposed application of SVTAS in nuclear magnetic resonance scan. (**F**) Six sentences of patient demand and (**G**) luminescent pix count from SVTAS corresponding to six sentences. (**H**) Classification test normalized confusion matrix for recognizing the six sentences in (F).

self-power ability. Reliant on triboelectrification and EL effect, TIEL is effective in converting gentle mechanical stimuli into real-time light emission, which provides an alternative route to the development of self-powered visualized sensors. An SVTAS based on an elaborated TIEL unit is obtained through a combination of high-modulus PVDF nanofibers, a high luminescent ZEPM layer, and a mesh electrode–enhanced layer with the capability of interfacial charge trapping. It can be applied to convert gentle tactile and acoustic wave stimuli into TIEL signals. In the process of tactile sensing under HS mode, the SVTAS exhibits a high brightness of 0.5 mW cm^{-2} (32 cd m^{-2}) and a record-low detection limit of 0.5 kPa, in which the high brightness is even discernible in an ambient illumination of 300 lux. Moreover, the SVTAS performs acoustic sensing at the highest response of 44.07 Hz and 60 to 90 dB, with a high SNR of 8.7 dB^{-1}, and an ultrafast response time of 0.8 ms under CS mode. Because of the excellent sensing performance of SVTAS, advanced artificial visualized perception systems can be constructed to recognize the motion trajectories and human speech with different information, which illustrates the huge potential of the SVTAS as a self-powered visualized sensor. Notably, replacement of each component layer with stretchable materials can make the SVTAS stretchable, which could be applied to many more emerging technologies, such as E-skin, wearable, and biomedical devices. This is worthwhile to further investigate in future. Therefore, this ultrasensitive and ultrafast SVTAS shows massive potential in the development of novel somatosensory and auditory artificial visualized perception systems and greatly expands the scope of applications for TIEL technique.

MATERIALS AND METHODS

Fabrication of the SVTAS

The ZnS:Cu particles (Shanghai Ke Yan Company) and PMMA solution (Longsheng Teco) were mixed at an appropriate ratio. After thorough mixing, it was coated onto the circular polyethylene glycol terephthalate plate with different diameters. The coated substrate was dried at room temperature for 3 hours, and then the obtained ZEPM film was removed from the substrate. Commercially available polyester screens were used for the screen-printing apparatus with a count of 100 mesh and a designed electrode window. Poly (3,4-ethylenedioxythiophene):poly(styrene sulfonate) conductive polymer ink (Orgacon, Agfa) was printed on the above-mentioned ZEPM film to obtain the transparent mesh-enhanced layer after 1 hour of annealing at 60°C. The PVDF nanofibers were prepared using the same solution and through the same electrospinning process as our previously reported (*34*). Last, the substrate, ZEPM film with the mesh-enhanced layer, and the triboelectrification layer of PVDF nanofibers were obtained through layer-by-layer sequential construction. Thus, SVTAS was obtained.

Measurements

All scanning electron microscopy images were captured by using a field-emission scanning electron microscope (Nova Nano 450, FEI). The contact pressure was evaluated by using a pressure sensor (Nano 17, ATI). Periodic mechanical traction was performed by a linear motor (E1100, LinMot) to generate TIEL signals. TIEL spectrum was observed under a spectrometer with a vertically arranged optical fiber collimating lens (Nova, Idea optics). TIEL emission was observed with the assistance of a Si photodetector (AM-F10, Keshengda) connected with an oscilloscope (TBS 1000C, Tektronix).

Statistical analysis

All results were analyzed at the sample size of $n \geq 3$. The data were presented as the mean values ± SD. Origin 8.0 was used for analysis.

Supplementary Materials

The PDF file includes:

Supplementary Text S1 to S6
Figs. S1 to S17
Table S1
Legends for movies S1 to S4

Other Supplementary Material for this manuscript includes the following:

Movies S1 to S4

REFERENCES AND NOTES

1. L. Gu, S. Poddar, Y. Lin, Z. Long, D. Zhang, Q. Zhang, L. Shu, X. Qiu, M. Kam, A. Javey, Z. Fan, A biomimetic eye with a hemispherical perovskite nanowire array retina. *Nature* **581**, 278–282 (2020).
2. T. Jiang, Y. Wang, Y. Zheng, L. Wang, X. He, L. Li, Y. Deng, H. Dong, H. Tian, Y. Geng, L. Xie, Y. Lei, H. Ling, D. Ji, W. Hu, Tetrachromatic vision-inspired neuromorphic sensors with ultraweak ultraviolet detection. *Nat. Commun.* **14**, 2281 (2023).
3. K. Qin, C. Chen, X. Pu, Q. Tang, W. He, Y. Liu, Q. Zeng, G. Liu, H. Guo, C. Hu, Magnetic array assisted triboelectric nanogenerator sensor for real-time gesture interaction. *Nanomicro Lett.* **13**, 51 (2021).
4. Y. H. Jung, T. X. Pham, D. Issa, H. S. Wang, J. H. Lee, M. Chung, B.-Y. Lee, G. Kim, C. D. Yoo, K. J. Lee, Deep learning-based noise robust flexible piezoelectric acoustic sensors for speech processing. *Nano Energy* **101**, 107610 (2022).
5. J. Qu, B. Mao, Z. Li, Y. Xu, K. Zhou, X. Cao, Q. Fan, M. Xu, B. Liang, H. Liu, X. Wang, X. Wang, Recent progress in advanced tactile sensing technologies for soft grippers. *Adv. Funct. Mater.* **33**, 2306249 (2023).
6. S. Min, D. H. Kim, D. J. Joe, B. W. Kim, Y. H. Jung, J. H. Lee, B.-Y. Lee, I. Doh, J. An, Y.-N. Youn, B. Joung, C. D. Yoo, H.-S. Ahn, K. J. Lee, Clinical validation of a wearable piezoelectric blood-pressure sensor for continuous health monitoring. *Adv. Mater.* **35**, 2301627 (2023).
7. Y. Zhang, X. Zhou, N. Zhang, J. Zhu, N. Bai, X. Hou, T. Sun, G. Li, L. Zhao, Y. Chen, L. Wang, C. F. Guo, Ultrafast piezocapacitive soft pressure sensors with over 10 kHz bandwidth via bonded microstructured interfaces. *Nat. Commun.* **15**, 3048 (2024).
8. S. Gong, B. Zhang, J. Zhang, Z. L. Wang, K. Ren, Biocompatible poly(lactic acid)-based hybrid piezoelectric and electret nanogenerator for electronic skin applications. *Adv. Funct. Mater.* **30**, 1908724 (2020).
9. Q. Zhou, B. Ji, F. Hu, Z. Dai, S. Ding, H. Yang, J. Zhong, Y. Qiao, J. Zhou, J. Luo, B. Zhou, Magnetized microcilia array-based self-powered electronic skin for micro-scaled 3D morphology recognition and high-capacity communication. *Adv. Funct. Mater.* **32**, 2208120 (2022).
10. D. J. Lu, T. Liu, X. J. Meng, B. Luo, J. X. Yuan, Y. H. Liu, S. Zhang, C. C. Cai, C. Gao, J. L. Wang, S. F. Wang, S. X. Nie, Wearable triboelectric visual sensors for tactile perception. *Adv. Mater.* **7**, 220917 (2023).
11. Y. Zhao, S. Gao, X. Zhang, W. Huo, H. Xu, C. Chen, J. Li, K. Xu, X. Huang, Fully flexible electromagnetic vibration sensors with annular field confinement origami magnetic membranes. *Adv. Funt. Mater.* **30**, 2001553 (2020).
12. B. Hou, L. Yi, C. Li, H. Zhao, R. Zhang, B. Zhou, X. Liu, An interactive mouthguard based on mechanoluminescence-powered optical fiber sensors for bite-controlled device operation. *Nat. Electron.* **5**, 682–693 (2022).
13. J. He, R. Wei, S. Ge, W. Wu, J. Guo, J. Tao, R. Wang, C. Wang, C. Pan, Artificial visual-tactile perception array for enhanced memory and neuromorphic computations. *InfoMat* **6**, e12493 (2023).
14. C. Li, N. Schramma, Z. Wang, N. F. Qari, M. Jalaal, M. I. Latz, S. Cai, Ultrasensitive and robust mechanoluminescent living composites. *Sci. Adv.* **9**, eadl8643 (2023).
15. R. Wei, J. He, S. Ge, H. Liu, X. Ma, J. Tao, X. Cui, X. Mo, Z. Li, C. Wang, C. Pan, Self-powered all-optical tactile sensing platform for user-interactive interface. *Adv. Mater. Technol.* **8**, 2200757 (2022).
16. B. Zhou, J. Liu, X. Huang, X. Qiu, X. Yang, H. Shao, C. Tang, X. Zhang, Mechanoluminescent-triboelectric bimodal sensors for self-powered sensing and intelligent control. *Nanomicro Lett.* **15**, 72 (2023).
17. B. Ren, B. Chen, X. Zhang, H. Wu, Y. Fu, D. Peng, Mechanoluminescent optical fiber sensors for human-computer interaction. *Sci. Bull.* **68**, 542–545 (2023).
18. X. Ma, C. Wang, R. Wei, J. He, J. Li, X. Liu, F. Huang, S. Ge, J. Tao, Z. Yuan, P. Chen, D. Peng, C. Pan, Bimodal tactile sensor without signal fusion for user-interactive applications. *ACS Nano* **16**, 2789–2797 (2022).

19. C. Pan, M. Chen, R. Yu, Q. Yang, Y. Hu, Y. Zhang, Z. L. Wang, Progress in piezo-phototronic-effect-enhanced light-emitting diodes and pressure imaging. *Adv. Mater.* **28**, 1535–1552 (2016).
20. Y. Zhang, R.-J. Xie, Mechanoluminescence rebrightening the prospects of stress sensing: A review. *Adv. Mater.* **33**, e2005925 (2021).
21. X. Wu, X. Zhu, P. Chong, J. Liu, L. N. Andre, K. S. Ong, K. Brinson Jr., A. I. Mahdi, J. Li, L. E. Fenno, H. Wang, G. Hong, Sono-optogenetics facilitated by a circulation delivered rechargeable light source for minimally invasive optogenetics. *Proc. Natl. Acad. Sci. U.S.A.* **116**, 26332–26342 (2019).
22. C. Wang, Y. Yu, Y. Yuan, C. Ren, Q. Liao, J. Wang, Z. Chai, Q. Li, Z. Li, Heartbeat-sensing mechanoluminescent device based on a quantitative relationship between pressure and emissive intensity. *Matter* **2**, 181–193 (2020).
23. Y. Zhuang, D. Tu, C. Chen, L. Wang, H. Zhang, H. Xue, C. Yuan, G. Chen, C. Pan, L. Dai, R.-J. Xie, Force-induced charge carrier storage: A new route for stress recording. *Light Sci. Appl.* **9**, 182 (2020).
24. S. Jeong, S. Song, K.-I. Joo, J. Kim, S.-H. Hwang, J. Jeong, H. Kim, Bright, wind-driven white mechanoluminescence from zinc sulphide microparticles embedded in a polydimethylsiloxane elastomer. *Energy Environ. Sci.* **7**, 3338–3346 (2014).
25. X. Qian, Z. Cai, M. Su, F. Li, W. Fang, Y. Li, X. Zhou, Q. Li, X. Feng, W. Li, X. Hu, X. Wang, C. Pan, Y. L. Song, Printable skin-driven mechanoluminescence devices via nanodoped matrix modification. *Adv. Mater.* **30**, 1800291 (2018).
26. X. Wang, M. Que, M. Chen, X. Han, X. Li, C. Pan, Z. L. Wang, Full dynamic-range pressure sensor matrix based on optical and electrical dual-mode sensing. *Adv. Mater.* **29**, 1605817 (2017).
27. C. Wang, R. Ma, D. Peng, X. Liu, J. Li, B. Jin, A. Shan, Y. Fu, L. Dong, W. Gao, Z. L. Wang, C. Pan, Mechanoluminescent hybrids from a natural resource for energy-related applications. *InfoMat* **3**, 1272–1284 (2021).
28. T. Zheng, M. Runowski, I. R. Matín, K. Soler-Carracedo, L. Peng, M. Skwierczyńska, M. Sójka, J. Barzowska, S. Mahlik, H. Hemmerich, F. Rivera-lópez, P. Kulpiński, V. Lavín, D. Alonso, D. Peng, Mechanoluminescence and photoluminescence heterojunction for superior multi-mode sensing platform of friction, force, pressure and temperature in fibers and 3D-printed polymers. *Adv. Mater.* **35**, 2304140 (2023).
29. X. Zhao, Z. Zhang, Q. Liao, X. Xun, F. Gao, L. Xu, Z. Kang, Y. Zhang, Self-powered user-interactive electronic skin for programmable touch operation platform. *Sci. Adv.* **6**, eaba4294 (2020).
30. X. Y. Wei, X. Wang, S. Y. Kuang, L. Su, H. Y. Li, Y. Wang, C. Pan, Z. L. Wang, G. Zhu, Dynamic triboelectrification-induced electroluminescence and its use in visualized sensing. *Adv. Mater.* **28**, 6656–6664 (2016).
31. H.-J. Park, S. Kim, J. H. Lee, H. T. Kim, W. Seung, Y. Son, T. Y. Kim, U. Khan, N.-M. Park, S.-W. Kim, Self-powered motion-driven triboelectric electroluminescence textile system. *ACS Appl. Mater. Interfaces* **11**, 5200–5207 (2019).
32. J. Li, Z. Zhang, X. Luo, L. Zhu, Z. L. Wang, Triboelectric leakage-field-induced electroluminescence based on ZnS:Cu. *ACS Appl. Mater. Interfaces* **14**, 4775–4782 (2022).
33. L. Su, Z. Wang, C. Lu, W. Ding, Y. Zhao, Y. Zi, Persistent triboelectrification-induced electroluminescence for self-powered all-optical wireless user identification and multi-mode anti-counterfeiting. *Mater. Horiz.* **10**, 2445–2454 (2023).
34. Z. Tian, L. Su, H. Wang, H. Q. Wang, Y. L. Zi, Underwater self-powered all-optical wireless ultrasonic sensing, positioning and communication with ultrafast response time and ultrahigh sensitivity. *Adv. Opt. Mater.* **10**, 2102091 (2022).
35. X. Pan, Y. Zhuang, W. He, C. Lin, L. Mei, C. Chen, H. Xue, Z. Sun, C. Wang, D. Peng, Y. Zheng, C. Pan, L. Wang, R.-J. Xie, Quantifying the interfacial triboelectricity in inorganic-organic composite mechanoluminescent materials. *Nat. Commun.* **15**, 2673 (2024).
36. G. Lee, S. Song, W. H. Jeong, C. Lee, J.-S. Kim, J.-H. Lee, J. M. Choi, H. Choi, Y. Kim, S. J. Lim, S. M. Jeong, Interfacial triboelectricity lights up phosphor-polymer elastic composites: Unraveling the mechanism of mechanoluminescence in zinc sulfide microparticle-embedded polydimethylsiloxane films. *Small* **25**, 2307089 (2024).
37. Y. Wang, H. L. Wang, H. Y. Li, X. Y. Wei, G. Zhu, Enhanced high-resolution triboelectrification-induced electroluminescence for self-powered visualized interactive sensing. *ACS Appl. Mater. Interfaces* **11**, 13796–13802 (2019).
38. H. Wang, L. Su, H. Li, Z. L. Wang, G. Zhu, Electret-induced electric field assisted luminescence modulation for interactive visualized sensing in a non-contact mode. *Mater. Horiz.* **7**, 1144–1149 (2020).
39. X. Y. Wei, H. Wang, Y. Wang, S. Y. Kuang, X. X. Zhu, J. Zou, L. Wang, X. Zeng, F. Rao, G. Zhu, Fully-integrated motion-driven electroluminescence enabled by triboelectrification for customized flexible display. *Nano Energy* **61**, 158–164 (2019).
40. L. Su, Q. Xiong, Y. Zhu, Y. Zi, A liquid–solid contact electrification based all-optical liquid flow sensor for microfluidic analysis in biomedical applications. *Adv. Funct. Mater.* **32**, 2207096 (2022).
41. S. Y. Zhang, Y. Zhu, Y. F. Xia, K. Liu, S. Li, B. Yang, M. Li, X. Zhi, X. Wang, Wearable Integrated self-powered electroluminescence display device based on all-in-one MXene electrode for information encryption. *Adv. Funct. Mater.* **33**, 2307609 (2003).
42. L. Su, Z. Y. Jiang, Z. Tian, H. Wang, H. Wang, Y. Zi, Self-powered, ultrasensitive, and high-resolution visualized flexible pressure sensor based on color-tunable triboelectrification-induced electroluminescence. *Nano Energy* **79**, 10543179 (2021).
43. L. Su, H. L. Wang, Z. Tian, H. Wang, Q. Cheng, W. Yu, Low detection limit and high sensitivity wind speed sensor based on triboelectrification-induced electroluminescence. *Adv. Sci.* **6**, 1901980 (2019).
44. X. J. Zhao, S. Y. Kuang, Z. L. Wang, G. Zhu, Electricity-free electroluminescence excited by droplet impact driven triboelectric field on solid-liquid interface. *Nano Energy* **75**, 104823 (2020).
45. Y. Chen, X. Wei, H. Li, Y. Fan, W. Hu, G. Zhu, Stretchable hybrid bilayered luminescent composite based on the combination of strain-induced and triboelectrification-induced electroluminescence. *ACS Omega* **4**, 20470–20475 (2019).
46. X. Y. Wei, L. Liu, H. L. Wang, S. Y. Kuang, X. Zhu, Z. L. Wang, Y. Zhang, G. Zhu, High-intensity triboelectrification-induced electroluminescence by microsized contacts for self-powered display and illumination. *Adv. Mater. Interfaces* **5**, 1701063 (2018).
47. C. Jia, Y. Xia, Y. Zhu, M. Wu, S. Zhu, X. Wang, High-brightness, high-resolution, and flexible triboelectrification-induced electroluminescence skin for real-time image and human-machine information interaction. *Adv. Funct. Mater.* **32**, 202201292 (2022).
48. L. Su, Q. Xiong, H. Y. Wang, Y. Zi, Porous-structure-promoted tribo-induced high-performance self-powered tactile sensor toward remote human-machine interaction. *Adv. Sci.* **9**, 2203510 (2022).
49. T. Bu, T. Xiao, Z. Yang, G. Liu, X. Fu, J. Nie, T. Guo, Y. Pang, J. Zhao, F. Xi, C. Zhang, Z. L. Wang, Stretchable triboelectric–photonic smart skin for tactile and gesture sensing. *Adv. Funct. Mater.* **16**, 1800066 (2018).
50. H. L. Wang, S. Y. Kuang, H. Y. Li, Z. L. Wang, G. Zhu, Large-area integrated triboelectric sensor array for wireless static and dynamic pressure detection and mapping. *Small* **16**, 1906352 (2020).

Acknowledgments

Funding: We thank the National Natural Science Foundation of China (grant nos. 52273282, 5227053344, 62304034, and 52275560), Guangdong Natural Science Funds for Distinguished Young Scholar (grant no. 2023B1515020074), HKSAR the Research Grants Council General Research Funds (grant no. 14202121), Hebei Natural Science Foundation (grant no. F2024501044), and Guangzhou-HKUST(GZ) Joint Funding Project (grant no. 2024A03J0466). This work was supported in part by the Project of Hetao Shenzhen-Hong Kong Science and Technology Innovation Cooperation Zone (HZQB-KCZYB-2020083). **Author contributions:** Conceptualization: L.S., S.K., and Y.Zi. Methodology: L.S., S.K., Y.Zhao, and Y.Zi. Investigation: L.S., S.K., Z.L.W., and Y.Zi. Visualization: J.L., G.Z., and L.S. Supervision: Y.Z., Z.L.W., and Y.Zi. Writing (original draft): L.S., S.K., and Y.Zi. Writing (review and editing): L.S., S.K., Y.Zhao, Z.L.W., and Y.Zi. **Author contributions:** The authors declare that they have no competing interests. **Data and materials availability:** All data needed to evaluate the conclusions in the paper are present in the paper and/or the Supplementary Materials.

Submitted 5 June 2024
Accepted 25 September 2024
Published 30 October 2024
10.1126/sciadv.adq8989